Research Article

Arginine modification of hybrid cobalt/nitrogen Ti$_3$C$_2$T$_x$ MXene and its application as a sulfur host for lithium-sulfur batteries

Miao Zhang[1], Kaiyu Zhang[1], Wei Wei[1], Hongxin Yuan[2], Jingjing Chang[1], Yue Hao[1]

[1]Academy of Advanced Interdisciplinary Research, Xidian University, Xi'an 710071, Shaanxi, China.
[2]School of Materials Science and Engineering, Nanyang Technological University, Singapore 639798, Singapore.

Correspondence to: Prof. Jingjing Chang, Academy of Advanced Interdisciplinary Research, Xidian University, 266 Xinglong Section of Xifeng Road, Xi'an 710126, Shaanxi, China. E-mail: jjingchang@xidian.edu.cn; Dr. Miao Zhang, Academy of Advanced Interdisciplinary Research, Xidian University, 266 Xinglong Section of Xifeng Road, Xi'an 710126, Shaanxi, China. E-mail: miaozhang@xidian.edu.cn

Abstract

The shuttling effect of lithium polysulfides (LiPSs) is one of the challenges facing the commercialization, which leads to a significant capacity degradation. This paper proposes a novel method to promote polysulfide transformation by employing arginine to regulate the layer spacing of cobalt-nitrogen doped Ti$_3$C$_2$T$_x$ MXene (Co-N@Ti$_3$C$_2$T$_{x-Arg}$). The results revealed that arginine effectively extended the interlayer spacing and promoted the homogeneous dispersion of Co and N atoms, thus endowing the sulfur host with a high catalytic activity during the charging and discharging processes. The extended interlayer spacing increased the specific surface area and captured sufficient LiPSs for subsequent catalytic conversions, while the Co and N doping on the surface of Ti$_3$C$_2$T$_x$ significantly promoted the rapid conversion of the LiPSs to Li$_2$S. Therefore, the S cathode coated with Co-N@Ti$_3$C$_2$T$_{x-Arg}$ exhibited an excellent cycling stability with a low-capacity fading rate of 0.083% over 200 cycles in addition to a high reversible capacity of 1,365.4 mAh g^{-1} at 0.1 C.

Keywords: Arginine, Co-N doped, Ti$_3$C$_2$T$_x$, Li-S batteries

INTRODUCTION

Lightweight and long service rechargeable batteries have been developed to satisfy the increasing demands of industrial needs, military progress and portable life[1-3]. Furthermore, the development of advanced electrochemical energy conversion and storage systems with a high energy density has been gaining significant attention[4-7]. Despite the various advantages of existing lithium-ion batteries, their low energy density based on the intercalation mechanism has severely hindered the scale-up fabrication of miniature batteries[5]. Lithium-sulfur (Li-S) batteries with high theoretical specific capacity (1,675 mAh g^{-1}) and energy density (2,567 Wh kg^{-1}) have attracted considerable attention as the next-generation batteries[8-11]. However, their low sulfur utilization, sluggish redox reaction kinetics, fast capacity fading, and low coulombic efficiency (CE) have hindered their commercialization[12,13].

To address these issues, several studies have reported the development of advanced sulfur host materials for the Li-S cathodes[14,15]. For example, carbon materials and conducting material with large specific surface area have been used to inhibit the shuttle effect of polysulfide. In particular, two-dimensional conductive carbon materials have been employed owing to their adjustable morphology and high electrical conductivity[16-18]. Nevertheless, the interactions are weak between polar lithium polysulfides (LiPSs) and the nonpolar hydrophobic carbon framework play a very limited role in slowing down the shuttle effect or preventing interfacial charge transfer, thus leading to sluggish reaction kinetics[17,19,20].

The application of $Ti_3C_2T_x$ MXene in electrochemical energy-storage applications has been gaining significant attention owing to their unique properties[21,22-25], where several studies have employed $Ti_3C_2T_x$ as an electrode substrate for Li-S batteries[24,26,27] owing to its inherent metallic conductivity ($\geq 3.4 \times 10^3$ S m^{-1}) which can effectively promote a rapid electron transfer. Furthermore, $Ti_3C_2T_x$ MXene has abundant active sites and a variety of surface functional groups which can not only anchor and catalyze the polysulfide lithium through the interaction between the metal and sulfur, but also accelerate the sulfur redox reaction. Despite these advantages, there are still two key challenges facing the optimization of its electrochemical performance[28,29]: (1) $Ti_3C_2T_x$ nanosheets are easily stacked, which reduces the specific surface area and leads to a decrease in the utilization rate of sulfur; and (2) the surface-active sites cannot easily catalyze the adsorption of large quantities of LiPSs.

Several strategies have focused on increasing the layer spacing and modifying the $Ti_3C_2T_x$ morphology with amino acids[30,31]. In particular, small molecules that influence $Ti_3C_2T_x$ can weaken the interlayer van der Waals forces and provide a greater interlayer advantage. Unlike large molecules and nanocarbon materials, small molecules do not introduce an insulation phase and avoid the hydrophobicity of the composite materials[32]. Therefore, there is an urgent need to find appropriate small molecules that can regulate the interlaminar structure and increase the surface area of $Ti_3C_2T_x$. In addition, the active elements, such as N, Co, Ni, can effectively improve the electrochemical performance of lithium sulfur batteries[33-35]. Consequently, an efficient method to treat the $Ti_3C_2T_x$ surface termination groups is highly desirable to further improve the electrochemical performance and increase the structural variety of $Ti_3C_2T_x$ based sulfur hosts.

This paper reports the fabrication of amino acid-regulated Co, N-doped $Ti_3C_2T_x$ (Co-N@$Ti_3C_2T_x$) substrates bearing multiple polysulfide anchoring sites, which are expected to impart a high polysulfide conversion activity and real capacity to Li-S batteries. The interlayer spacing of $Ti_3C_2T_x$ was extended via an amino acid modification. Arginine, serine, and lysine were employed to obtain $Ti_3C_2T_{x\text{-Arg}}$, $Ti_3C_2T_{x\text{-Ser}}$, and $Ti_3C_2T_{x\text{-Lys}}$, respectively. The effect of the amino acid chain length on the interlayer spacing of $Ti_3C_2T_x$ was investigated. Finally, the possible application of each of the Co-N@$Ti_3C_2T_{x\text{-Arg}}$, Co-N@$Ti_3C_2T_{x\text{-Ser}}$, and Co-N@$Ti_3C_2T_{x\text{-Lys}}$

composites as an S host was assessed. The results revealed that the interlayer spacing of $Ti_3C_2T_x$ increased with an increase in the amino acid chain length. The Co-N@$Ti_3C_2T_{x-Arg}$ composites exhibited a stronger adsorption for LiPSs via the Co, N active site which suppressed the LiPSs shuttle effect and catalyzed the redox reaction. Consequently, the application of the Co-N@$Ti_3C_2T_{x-Arg}$ composite as a host of S cathode delivered a capacity of 1,365 mAh g^{-1} and exhibited stable cycles with a capacity fading rate of 0.083% per cycle over 200 cycles at 0.2 C.

MATERIALS AND METHODS

Materials
400 mesh powder of Ti_3AlC_2 was from XF Nano Technology Co., Ltd. (Nanjing, China), while serine, lysine, arginine, LiF, 4-dimethylaminopyridine (DMAP) and 1-(3-(dimethylamino) propyl)-3-ethylcarbimide hydrochloride (EDC), cobalt chloride hexahydrate were purchased from Titan Scientific Co., Ltd. (General-Reagent brand). Concentrated HCl (36.5%) was obtained from Sinopharm Chemical Reagent Co., Ltd.

Preparation of the $Ti_3C_2T_{x-Arg}$, $Ti_3C_2T_{x-Ser}$, $Ti_3C_2T_{x-Lys}$ composites
The $Ti_3C_2T_x$ composites were prepared using the LiF/HCl selective etching process previously reported by Gogotsi and Barsoum[36]. In a Teflon beaker, HCl (40 mL, 12 mol/L) was mixed with LiF (3.2 g) and Ti_3AlC_2 (2 g) was then slowly added. The mixture was stirred for 48 h at 45 °C. After etching, a washing process was performed to obtain $Ti_3C_2T_{x-Arg}$. The $Ti_3C_2T_x$ was modified by arginine via an esterification reaction[37] Arginine (0.045 g) was added to a suspension of $Ti_3C_2T_x$ (containing 0.09 g of $Ti_3C_2T_x$). The 0.0025 g EDC and DMAP as composite catalyst (mass ratio of 1:1) was mixed with arginine/$Ti_3C_2T_x$ suspension. The reaction temperature was up to 100 °C for 3 h, and the $Ti_3C_2T_{x-Arg}$ film was finally obtained by vacuum filtration. $Ti_3C_2T_{X-Ser}$ and $Ti_3C_2T_{X-Lys}$ were also obtained using the same method.

Preparation of the Co-N@$Ti_3C_2T_{x-Arg}$ @S cathode
Each of the $Ti_3C_2T_{X-Arg}$, $Ti_3C_2T_{X-Ser}$, and $Ti_3C_2T_{X-Lys}$ film was immersed in a $CoCl_2$ solution (0.1 mol·L^{-1}) for 2 h. After drying, each film was then annealed at 600 °C under an Ar atmosphere for 4 h (temperature rise of 5 °C /min) to obtain the Co-N@$Ti_3C_2T_{X-Arg}$, Co-N@$Ti_3C_2T_{X-Ser}$, and Co-N@$Ti_3C_2T_{X-Lys}$ films, respectively.

The S composite cathode was prepared as follows
The Co-N@$Ti_3C_2T_{x-Arg}$ was cut into diameter of 11 mm. An S/CS_2 solution (obtained by dissolving 20 mg of sulfur in 2 mL of CS_2) was then added dropwise to the film. After drying, the Co-N@$Ti_3C_2T_{X-Arg}$@S was heated at 155 °C for 6 h.

Characterization
The morphologies were imaged by a scanning electron microscope (SEM, ZEISS Sigma 300) at an increased voltage of 3 kV equipped with an energy-dispersive spectrometer (EDS, Oxford Xplore50, pure gold target with an accelerated voltage of 0.02 to 30 kV). The X-ray diffraction (XRD) patterns were recorded on a Rigaku Smart Lab (Japan) equipped with a CuKα light source (λ = 0.15406 nm). Samples were scanned in the diffraction angle (2θ) range of 5° to 60° at a scanning rate of 2°/min. The X-ray photoelectron spectroscopy (XPS) spectra were recorded on a Thermo Scientific K-Alpha model spectrometer. The entire spectral scan was performed with a universal energy of 100 eV and a step size of 1 eV. The Thermo Fisher DXR 2xi model Raman imaging microscope with a spectral resolution of less than 1.5 cm^{-1} was used for the Raman spectroscopy analysis.

Electrochemical measurements
The mass of sulfur in the electrode was in the range of 1.0-1.5 mg. The discs were then tested with CR2032 coin-type cells using lithium metal as the anode, Celgard 2400 as the separator, and the electrolyte solution

was composed of a LiTFSI (1 M) dissolved in a solution of 1,3-dioxolane (DOL) and dimethoxymethane (DME) (v:v = 1:1) solution containing $LiNO_3$ (1 wt.%) as the additive. The Charge and discharge measurements were conducted in the potential range of 1.5-3.0 V (*vs.* Li/Li$^+$) on a LAND testing system. electrolyte amount was 20 μL mg^{-1}. The cyclic voltammetry (CV) and electrochemical impedance spectroscopy (EIS) were conducted using DE7000 potentiostat/galvanostat in the frequency range of 10 kHz to 0.1 Hz.

RESULTS AND DISCUSSION

Figure 1 illustrates the procedure for the synthesis of the Co-N@$Ti_3C_2T_{x-Ser}$, Co-N@$Ti_3C_2T_{x-Lys}$, and Co-N@$Ti_3C_2T_{x-Arg}$ composites as a sulfur host. $Ti_3C_2T_x$ was obtained by selectively etching Ti_3AlC_2 by HCl/LiF to remove the Al atomic layer. Serine, lysine, and arginine (with different chain lengths) were chosen as the interlayer regulators owing to their dual function of being a nitrogen source and widening the $Ti_3C_2T_x$ layer spacing. The nitrogen-source-modified $Ti_3C_2T_x$ was used to build a self-supporting electrode and the self-supporting film was then successfully assembled by vacuum filtration. $CoCl_2$ was deposited onto the $Ti_3C_2T_x$ film by soaking, and Co and N were doped into the $Ti_3C_2T_x$ film after annealing. As the cathode substrate of Li-S batteries, Co-N@$Ti_3C_2T_{x-Arg}$ did not only extend the spacing of the nanosheets, but also increased the number of catalytic active sites.

The SEM results of the Ti_3AlC_2 and etched multilayer $Ti_3C_2T_x$ (Mul-$Ti_3C_2T_x$) are shown in Figure 2A and B, respectively, while those of $Ti_3C_2T_{X-Ser}$, $Ti_3C_2T_{X-Lys}$, and $Ti_3C_2T_{x-Arg}$, are shown in Figure 2C-E, respectively. The surface of Co-N@$Ti_3C_2T_{x-Arg}$ [Figure 2F] exhibited some roughness which can be attributed to the capillarity of thermal annealing. Cross sectional SEM images show that the thickness of the Co-N@$Ti_3C_2T_{x-Arg}$ (31.6 μm) is a few high than that of Co-N@$Ti_3C_2T_{x-Ser}$ and Co-N@$Ti_3C_2T_{x-Lys}$ (29.2, 30.8 μm) due to longer chain of arginine [Supplementary Figure 1]. Figure 2G represents the SEM/EDS image of Co-N@$Ti_3C_2T_{X-Arg}$. The results [Figure 2H-J] revealed a uniform distribution of N and Co, thus indicating the successful modification of $Ti_3C_2T_x$ by the amino acid and cobalt dichloride. The homogeneous distribution of elements Co throughout Co-N@$Ti_3C_2T_{x-Arg}$ was visualized by EDS elemental mapping [Supplementary Figure 2]. The EDS spectral images of Co-N@$Ti_3C_2T_{X-Ser}$ and Co-N@$Ti_3C_2T_{X-Lys}$ [Supplementary Figures 3 and 4] also confirmed the successful doping of Co and N into the $Ti_3C_2T_x$ composites. Nevertheless, the layer space of the Ser-, Lys-, and Arg-modified $Ti_3C_2T_x$ nanosheets varied, and the crumpling increased with an increase in the amino acid chain length. The XRD pattern of the raw material $Ti_3C_2T_x$ [Supplementary Figure 5] matched with the JCPDS data card. The disappearance of the (104) diffraction peak from the XRD pattern after HCl/LiF etching confirmed that most of the Al in the MAX material was successfully etched.

The schematic representation of the amino-acid-modified $Ti_3C_2T_x$ composites with LiF/HCl etching process [Figure 3A] revealed the abundant presence of hydroxyl groups in surface of $Ti_3C_2T_x$, which can interact with the abundant hydroxyl sites of amino acids to obtain the Co-$Ti_3C_2T_{x-Ser}$, Co-$Ti_3C_2T_{x-Lys}$, and Co-$Ti_3C_2T_{x-Arg}$ composites by esterification. The carboxyl groups of the amino acids and the hydroxyl groups on $Ti_3C_2T_x$ were esterified to form longer surface groups on the $Ti_3C_2T_X$, which is consistent with the morphological changes observed by SEM. Figure 3B shows the XRD patterns of Co-$Ti_3C_2T_{x-Ser}$, Co-$Ti_3C_2T_{x-Lys}$, Co-$Ti_3C_2T_{x-Arg}$, and multilayer MXene (Mul-$Ti_3C_2T_x$) composites. For $Ti_3C_2T_X$, the position of the characteristic (002) peak reflected the size of the layer spacing[38]. The corresponding characteristic angles of the (002) crystal planes of Co-$Ti_3C_2T_{X-Ser}$, Co-$Ti_3C_2T_{X-Lys}$, and Co-$Ti_3C_2T_{X-Arg}$ were at 6.47°, 6.3°, and 6.11°, respectively, and the values of the layer spacing obtained by the Bragg equation (*2d sin θ = nλ*) were 1.37, 1.4, and 1.45 nm, respectively, where *d* is the distance between the crystal faces, *λ* is the wavelength of the X-ray (*λ* = 0.15406 nm), *θ* is the angle between the corresponding crystal faces and the incident X-ray, *n*

Figure 1. Schematic representation of the synthesis of the Co-N@Ti$_3$C$_2$T$_x$ composites.

Figure 2. SEM images of the (A and B) multilayer Ti$_3$C$_2$T$_x$, (C-E) Ti$_3$C$_2$T$_{X\text{-Ser}}$, and Ti$_3$C$_2$T$_{X\text{-Lys}}$, and Ti$_3$C$_2$T$_{x\text{-Arg}}$, composites; (F-J) SEM image and EDS spectrum mapping: C, Co, and N elemental distribution of the Co-N@Ti$_3$C$_2$T$_{x\text{-Arg}}$ composite.

is the diffraction series (generally 1), thus indicating that the layer spacing can be effectively increased by an amino acid modification. The Raman spectra of the modified Co-N@Ti$_3$C$_2$T$_x$ were aligned with that of Mul-MXene [Figure 3C]. The spectra revealed that the intensities of Co-N@Ti$_3$C$_2$T$_{X\text{-Ser}}$, Co-N@Ti$_3$C$_2$T$_{X\text{-Lys}}$, and Co-N@Ti$_3$C$_2$T$_{x\text{-Arg}}$ gradually increased which can be attributed to the change in the surface roughness of the nanosheets after annealing, which is consistent with the SEM results. A disordered carbon (D band) and in-plane vibrations (G band) characteristic peaks was existed at 1,350 and 1,590 cm^{-1}[39]. A comparison of the D- and G-peak intensities for Mul-Ti$_3$C$_2$T$_X$ and the amino acid-modified Ti$_3$C$_2$T$_X$ nanosheets revealed that

Figure 3. (A) Schematic illustration of the $Ti_3C_2T_x$ modified by the amino acids. (B) XRD patterns of the $Co-Ti_3C_2T_{x-Ser}$, $Co-Ti_3C_2T_{x-Lys}$, $Co-Ti_3C_2T_{x-Arg}$, and $Mul-Ti_3C_2T_x$ composites. (C) Raman spectra of the $Co-N@Ti_3C_2T_{x-Ser}$, $Co-N@Ti_3C_2T_{x-Lys}$, $Co-N@Ti_3C_2T_{x-Arg}$, and $Mul-Ti_3C_2T_x$ composites from 0 to 3,250 cm^{-1}. (D) C 1s XPS spectrum of the crumpled $Co-N@Ti_3C_2T_{x-Arg}$ composite. (E) O 1s spectrum of the $Co-N@Ti_3C_2T_{x-Arg}$ composite. (F) Co 2p spectrum of the $Co-N@Ti_3C_2T_{x-Arg}$ composite. (G) N 1s spectrum of the $Co-N@Ti_3C_2T_{x-Arg}$ composite. (H) Ti 2p spectrum of the $Co-N@Ti_3C_2T_{x-Arg}$ composite.

the D-peak to G-peak intensity ratio (I_D/I_G) of Mul-MXene was higher than those of the amino acid-modified $Ti_3C_2T_X$, thus indicating that Mul-MXene has more carbon vacancies or larger graphitic regions, which confirmed the doping of nitrogen atoms by replacing some carbon atoms in the $Ti_3C_2T_x$ after pyrolysis. The surface chemical composition of $Co-N@Ti_3C_2T_x$ was further characterized by XPS. In comparison with the XPS spectrum of $Mul-Ti_3C_2T_x$ nanosheets [Supplementary Figure 6], the peaks at 779.8 and 400 eV indicated the presence of N and Co on the $Ti_3C_2T_X$, respectively[24]. The C 1s spectra [Figure 3D, Supplementary Figures 7 and 8] revealed the presence of five peaks at approximately 281.8, 284.6, 285.2, 286.1, and 288.5 eV corresponding to the C-Ti, C-C, C-N, C-O, and O=C-O bonds, respectively. The disappearance of the C-Ti-O bond in the modified $Ti_3C_2T_x$ compared to that of Mul-$Ti_3C_2T_x$ confirmed the reaction of amino acids with the-OH functional group on the $Ti_3C_2T_x$ surface. The additional C-N bond confirmed the interaction between the three amino acids and $Ti_3C_2T_X$. The O 1s spectra [Figure 3E, Supplementary Figures 7 and 8] revealed the presence of three peaks at approximately 529.2, 530.7, and 532.2 eV attributed to the presence of Co-O, O-C=O, and oxygen vacancies, respectively. The Co 2p spectra [Figure 3F, Supplementary Figures 7 and 8] were decomposed into two distinct peaks, Co 2p3/2 (780.2 eV) and Co 2p1/2 (795.7 eV), thus confirming the successful modification of the cobaltous oxide (CoO) nanoparticles in the three different pleated MXene nanosheets. The high-resolution N 1 s spectra [Figure 3G, Supplementary Figures 7 and 8] revealed the presence of pyridinic-N (397.5 eV), pyrrolic-N (398.3 eV), and quaternary-N (400.6 eV) in the $Co-N@Ti_3C_2T_{X-Ser}$, $Co-N@Ti_3C_2T_{X-Lys}$, and $Co-N@Ti_3C_2T_{x-Arg}$ composites, thus confirming that N was doped into $Ti_3C_2T_x$ rather than being present as a residue or impurity. The $Co-N@Ti_3C_2T_{X-Ser}$ composite was composed of 48.65% Ti-N bond, 16.2% pyrrolic N, and 35.14% pyridinic N, while the $Co-N@Ti_3C_2T_{X-Lys}$ composite was composed of 24.24% Ti-N bond,

30.30% pyrrolic N, and 45.45% pyridinic N. The Co-N@Ti$_3$C$_2$T$_{x\text{-Arg}}$ composite was composed of 11.11% Ti-N bond, 59.26% pyrrolic N, and 11.11% pyridinic N[40]. The proportion of the Ti-N bonds decreased with an increase in the amino acid chain length, which can be attributed to a mount of NH$_3$ being produced during metal doping, which reduced the number of generated Ti-N bonds. Binding energy and affinity of polar titanium with elemental sulfur (S8) and polar polysulfide (Li$_2$S$_n$, $4 \leq n \leq 8$) can be effectively enhanced by strong Lewis acid-base interactions with pyridine N and pyrrole N[41]. The Ti 2p spectra [Figure 3H, Supplementary Figures 7 and 8] revealed three Ti 2p1/2/ Ti 2p3/2 double bonds: Ti-O (465.7/458.7 eV, 465.6/459.6 eV, 464.2/458.1 eV), Ti-N (462.6/456.4 eV, 462.6/456.7 eV, 463.8/457.6 eV), and Ti-C (461.2/ 455.4 eV, 461.5/455.5 eV, 461.2/454.5 eV), respectively. Compared to the pure Ti$_3$C$_2$T$_X$, the Ti-O bonding in the Co-N@Ti$_3$C$_2$T$_{X\text{-Ser}}$, Co-N@Ti$_3$C$_2$T$_{X\text{-Lys}}$, and Co-N@Ti$_3$C$_2$T$_{x\text{-Arg}}$ composites increased, which can effectively anchor polysulfides. The Ti-O bond content initially increased and then decreased, indicating the Co-N@Ti$_3$C$_2$T$_{X\text{-Ser}}$, Co-N@Ti$_3$C$_2$T$_{X\text{-Lys}}$ and Co-N@Ti$_3$C$_2$T$_{x\text{-Arg}}$ have different degrees of oxidation during synthesis.

The possibility to employ each of the obtained composites as an S cathode was then investigated [Figure 4]. Free-standing Co-N@Ti$_3$C$_2$T$_{x\text{-Arg}}$ films were obtained by vacuum filtration and exhibited excellent flexibility [Supplementary Figure 9]. A representation of the application of Co-N@Ti$_3$C$_2$T$_{X\text{-Arg}}$/S electrodes in Li-S batteries is shown in Figure 4A, while the rate capabilities of Co-N@Ti$_3$C$_2$T$_{X\text{-Ser}}$/S, Co-N@Ti$_3$C$_2$T$_{X\text{-Lys}}$/S and Co-N@Ti$_3$C$_2$T$_{X\text{-Arg}}$/S electrodes are shown in Figure 4B. Specifically, the Co-N@Ti$_3$C$_2$T$_{X\text{-Arg}}$/S electrode exhibited the highest rate performance with initial discharge capacities of 1,365.0, 1,246.4, 1,305.3, 1,020.9, and 856.5 mAh g^{-1} at current rates in the range of 0.1 to 2 C. Even at 0.2 C, a high specific capacity of 1,359.9 mAh g^{-1} was maintained, thus indicating an outstanding electrochemical reversibility. The Co-N@Ti$_3$C$_2$T$_{X\text{-Arg}}$/S electrode demonstrated a better performance than the Mul-Ti$_3$C$_2$T$_x$/S, Co-N@Ti$_3$C$_2$T$_{X\text{-Ser}}$/S and Co-N@Ti$_3$C$_2$T$_{X\text{-Lys}}$/S electrodes at different rates, thus indicating the significance of the strong adsorption ability of LiPSs, which facilitated the efficient capture of the dissolved LiPSs for subsequent conversions and effectively suppressed the shuttle effect. The rate capability of Mul-Ti$_3$C$_2$T$_x$ composite cathode in Supplementary Figure 10 shows lower discharge capacity than Co-N@Ti$_3$C$_2$T$_{x\text{-Arg}}$, indicating Co-N@Ti$_3$C$_2$T$_{x\text{-Arg}}$ can effectively promote LiPSs conversion. Supplementary Figure 11 shows the discharge/ charge curves of the Co-N@Ti$_3$C$_2$T$_{X\text{-Ser}}$/S, Co-N@Ti$_3$C$_2$T$_{X\text{-Lys}}$/S, and Co-N@Ti$_3$C$_2$T$_{X\text{-Arg}}$/S composite electrodes at 0.2 C, the Co-N@Ti$_3$C$_2$T$_{X\text{-Arg}}$/S composite electrodes display two stable voltage platforms. The long-term cycling performances of the batteries at different rates were then investigated. The cycling performance of Co-N@Ti$_3$C$_2$T$_{X\text{-Ser}}$/S, Co-N@Ti$_3$C$_2$T$_{X\text{-Lys}}$/S, and Co-N@Ti$_3$C$_2$T$_{X\text{-Arg}}$/S was tested at 0.2 C (1.0 C = 1,675 mAh g^{-1}, based on sulfur). The results [Figure 4C] revealed that the Co-N@Ti$_3$C$_2$T$_{X\text{-Arg}}$/S composite sulfur electrodes showed a high initial specific capacity of 1,314.3 mAh g^{-1} at 0.2 C, Furthermore, a high specific (1,098 mAh g^{-1}) was maintained (corresponding to a capacity retention rate of 84.1%) and the corresponding decay rate per cycle was 0.083% after 200 cycles, while the Co-N@Ti$_3$C$_2$T$_{X\text{-Ser}}$/S and Co-N@Ti$_3$C$_2$T$_{X\text{-Lys}}$/S electrodes delivered low initial capacities of 539.5 and 200 mAh g^{-1}, respectively. And the areal capacity Co-N@Ti$_3$C$_2$T$_{x\text{-Ser}}$/S, Co-N@Ti$_3$C$_2$T$_{X\text{-Lys}}$/S, and Co-N@Ti$_3$C$_2$T$_{x\text{-Arg}}$/S are shown in Supplementary Figure 12. The CE of the Co-N@Ti$_3$C$_2$T$_{X\text{-Arg}}$/S electrodes [Figure 4D], was stabilized at a high value of 99.6%, whereas those of the Co-N@Ti$_3$C$_2$T$_{X\text{-Ser}}$/S and Co-N@Ti$_3$C$_2$T$_{X\text{-Lys}}$/S electrodes fluctuated. The reason is that there are more active sites on Ti$_3$C$_2$T$_x$ surface, which can effectively inhibit the dissolution of LiPSs into the electrolyte and reduce the shuttle phenomenon, this improves the utilization of S8. To further compare the electrochemical performance of Co-N@Ti$_3$C$_2$T$_{X\text{-Ser}}$/S, Co-N@Ti$_3$C$_2$T$_{X\text{-Lys}}$/S, and Co-N@Ti$_3$C$_2$T$_{X\text{-Arg}}$/S electrodes, the EIS experiments were conducted in the frequency range of 100 kHz to 10 mHz [Figure 4E], all of them show the high-frequency region and the low-frequency region, where R_Ω is the electrolyte impedance and Rct is the charge transfer resistance. The charge transfer resistance was 15.7, 19.8 and 36.3 Ω for Co-N@Ti$_3$C$_2$T$_{X\text{-Ser}}$/S, Co-N@Ti$_3$C$_2$T$_{X\text{-Lys}}$/S, and Co-N@Ti$_3$C$_2$T$_{X\text{-Arg}}$/S composite cathode, respectively. The results revealed that Co-N@Ti$_3$C$_2$T$_{x\text{-Arg}}$/S composite cathode has highest charge transfer resistance, which due to that long chain
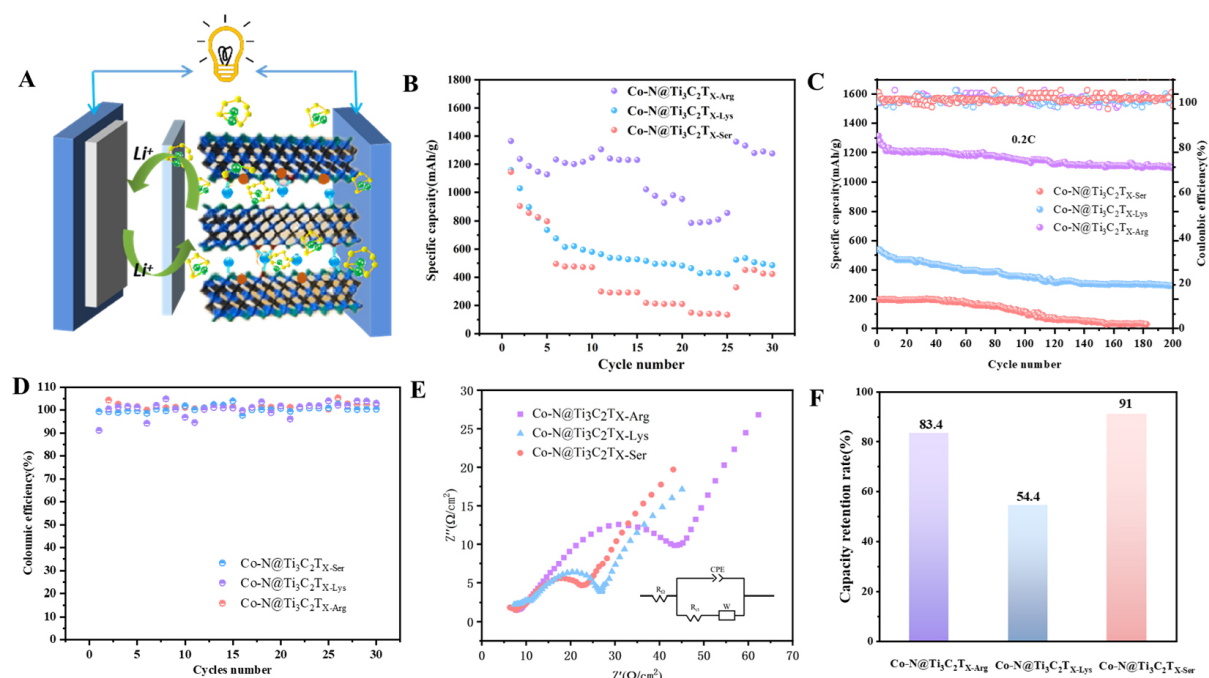
Figure 4. (A) Schematic illustration of the fabrication of the Co-N@Ti$_3$C$_2$T$_{X-Arg}$/S electrodes for Li-S batteries. (B) Rate performances of the Co-N@Ti$_3$C$_2$T$_{X-Ser}$/S, Co-N@Ti$_3$C$_2$T$_{X-Lys}$ /S, and Co-N@Ti$_3$C$_2$T$_{X-Arg}$/S electrodes. (C) Long-term cycling of the Co-N@Ti$_3$C$_2$T$_{X-Ser}$/S, Co-N@Ti$_3$C$_2$T$_{X-Lys}$/S, and Co-N@Ti$_3$C$_2$T$_{X-Arg}$/S electrodes. (D) CEs of the Co-N@Ti$_3$C$_2$T$_{X-Ser}$/S, Co-N@Ti$_3$C$_2$T$_{X-Lys}$ /S and Co-N@Ti$_3$C$_2$T$_{X-Arg}$/S electrodes at different rates. (E) Nyquist plots of the Co-N@Ti$_3$C$_2$T$_{X-Ser}$/S, Co-N@Ti$_3$C$_2$T$_{X-Lys}$ /S and Co-N@Ti$_3$C$_2$T$_{X-Arg}$/S electrodes, and the inset shows the equivalent circuit and fitted results. (F) Decay rates of the Co-N@Ti$_3$C$_2$T$_{X-Ser}$/S, Co-N@Ti$_3$C$_2$T$_{X-Lys}$/S and Co-N@Ti$_3$C$_2$T$_{X-Arg}$/S electrodes.

amino acids increased layer spacing and reduced interlayer connectivity. However, discharge capacity is affected by many factors, including the number of active sites, lamellar morphology, etc, large layer spacing exposes more catalytic sites, effectively catalyzing and inhibiting the shuttle effect of polysulfide. Therefore, Co-N@Ti$_3$C$_2$T$_{X-Arg}$/S electrode exhibits higher discharge capacity. These findings reflect the enhanced lithium ion transport and low resistance of electrolytes of the Co-N@Ti$_3$C$_2$T$_{X-Lys}$/S electrodes during an electrochemical operation. Figure 4F shows the decay rate of the Co-N@Ti$_3$C$_2$T$_{X-Ser}$/S, Co-N@Ti$_3$C$_2$T$_{X-Lys}$/S, and Co-N@Ti$_3$C$_2$T$_{X-Arg}$/S electrodes, where the Co-N@Ti$_3$C$_2$T$_{X-Arg}$/S electrode exhibited an excellent performance with a high-capacity retention of 83.4%, However, the other two composites exhibited retentions of 54.4% and 91.0% (the initial capacity is only 200 mAh g^{-1}). Compare previous articles of MXene-based as host materials, the performance of Co-N@Ti$_3$C$_2$T$_{x-Arg}$/S electrodes have significant improvement [Supplementary Table 1]. The excellent electrochemical performance obtained with the Co-N@Ti$_3$C$_2$T$_{X-Arg}$/S composite sulfur electrodes is mainly attributed to the synergistic effect of the strong adsorption and excellent catalytic activity achieved by the increased active site for the sulfur electrodes.

CONCLUSIONS

This study reported the synthesis of Co, N doped Ti$_3$C$_2$T$_x$ MXene via thermal annealing of arginine-modified and CoCl$_2$-deposited Ti$_3$C$_2$T$_x$. The long molecular chain of arginine effectively increased the layer spacing of the Ti$_3$C$_2$T$_x$ nanosheets. Once applied to Li-S batteries, the Co-N@Ti$_3$C$_2$T$_{x-Arg}$ composite sulfur electrodes exhibited an electrochemical performance which was higher than those of Co-N@Ti$_3$C$_2$T$_{X-Ser}$ and Co-N@Ti$_3$C$_2$T$_{X-Lys}$ composite sulfur electrodes since the exposed active site effectively promoted the chemisorption of LiPSs. The Co-N@Ti$_3$C$_2$T$_{x-Arg}$ composite sulfur electrode exhibited an initial discharge specific capacity of 1,314.3 mAh g^{-1} and a reversible specific capacity that was maintained at 1,096 mAh g^{-1} at

0.2 C even after 200 cycles. The results of this study revealed that combining amino acids with the highly conductive $Ti_3C_2T_x$ can enable the development of promising small-molecule-modified ultrathin 2D materials which can be employed in high-performance Li-S batteries.

DECLARATIONS

Authors' contributions
Synthesis and testing of materials, data collection, original manuscript writing: Zhang M
Validation and original manuscript revision: Zhang K
Data analysis: Wei W
manuscript Revision: Yuan H
Reviewing and editing: Chang J
Revision: Hao Y

Availability of data and materials
According to reasonable requirements, all of the data examined in this research can be obtained from the correspondents.

Conflicts of interest
All authors declared that there are no conflicts of interest.

Ethical approval and consent to participate
Not applicable.

Consent for publication
Not applicable.

REFERENCES

1. Chang P, Mei H, Zhou S, Dassios KG, Cheng L. 3D printed electrochemical energy storage devices. *J Mater Chem A* 2019;7:4230-58. DOI
2. Xia J, Gao R, Yang Y, et al. Ti_nO_{2n-1}/MXene hierarchical bifunctional catalyst anchored on graphene aerogel toward flexible and high-energy Li-S batteries. *ACS Nano* 2022;16:19133-44. DOI
3. Liu K, Fan Y, Ali A, Shen PK. A flexible and conductive MXene-coated fabric integrated with in situ sulfur loaded MXene nanosheets for long-life rechargeable Li-S batteries. *Nanoscale* 2021;13:2963-71. DOI PubMed
4. Chang P, Mei H, Zhao Y, Huang W, Zhou S, Cheng L. 3D structural strengthening urchin-like $Cu(OH)_2$-based symmetric supercapacitors with adjustable capacitance. *Adv Funct Mater* 2019;29:1903588. DOI
5. Chang P, Mei H, Zhang M, et al. 3D printed electrochromic supercapacitors with ultrahigh mechanical strength and energy density. *Small* 2021;17:e2102639. DOI
6. Song MK, Zhang Y, Cairns EJ. A long-life, high-rate lithium/sulfur cell: a multifaceted approach to enhancing cell performance. *Nano Lett* 2013;13:5891-9. DOI PubMed
7. Xu T, Du H, Liu H, et al. Advanced nanocellulose-based composites for flexible functional energy storage devices. *Adv Mater* 2021;33:e2101368. DOI

8.   Zhong X, Wang D, Sheng J, et al. Freestanding and sandwich MXene-based cathode with suppressed lithium polysulfides shuttle for flexible lithium-sulfur batteries. *Nano Lett* 2022;22:1207-16. DOI

9.   Peng HJ, Zhang G, Chen X, et al. Enhanced electrochemical kinetics on conductive polar mediators for lithium-sulfur batteries. *Angew Chem Int Ed* 2016;55:12990-5. DOI

10.   Huang Z, Zhu Y, Kong Y, et al. Efficient synergism of chemisorption and wackenroder reaction via heterostructured La_2O_3-$Ti_3C_2T_x$-embedded carbon nanofiber for high-energy lithium-sulfur pouch cells. *Adv Funct Mater* 2023;33:2303422. DOI

11.   Nam S, Kim J, Nguyen VH, et al. Collectively exhaustive MXene and graphene oxide multilayer for suppressing shuttling effect in flexible lithium sulfur battery. *Adv Mater Technol* 2022;7:2101025. DOI

12.   Li H, Shao F, Wen X, et al. Graphene/MXene fibers-enveloped sulfur cathodes for high-performance Li-S batteries. *Electrochim Acta* 2021;371:137838. DOI

13.   Qiu Y, Li W, Zhao W, et al. High-rate, ultralong cycle-life lithium/sulfur batteries enabled by nitrogen-doped graphene. *Nano Lett* 2014;14:4821-7. DOI

14.   Hu B, Xu J, Fan Z, et al. Covalent organic framework based lithium-sulfur batteries: materials, interfaces, and solid-state electrolytes. *Adv Energy Mater* 2023;13:2203540. DOI

15.   Zheng Z, Ye H, Guo Z. Recent progress on pristine metal/covalent-organic frameworks and their composites for lithium-sulfur batteries. *Energy Environ Sci* 2021;14:1835-53. DOI

16.   Zheng X, Tang J, Wang P, Wang Z, Zou L, Li C. Interfused core-shell heterogeneous graphene/MXene fiber aerogel for high-performance and durable electromagnetic interference shielding. *J Colloid Interface Sci* 2022;628:994-1003. DOI

17.   Liu Y, He P, Zhou H. Rechargeable solid-state Li-air and Li-S batteries: materials, construction, and challenges. *Adv Energy Mater* 2018;8:1701602. DOI

18.   Li Z, Huang Y, Yuan L, Hao Z, Huang Y. Status and prospects in sulfur-carbon composites as cathode materials for rechargeable lithium-sulfur batteries. *Carbon* 2015;92:41-63. DOI

19.   Zhao Q, Zhu Q, Liu Y, Xu B. Status and prospects of MXene-based lithium-sulfur batteries. *Adv Funct Mater* 2021;31:2100457. DOI

20.   Feng Y, Liu H, Lu Q. From non-carbon host toward carbon-free lithium-sulfur batteries. *Nano Res* 2023;17:1337-65. DOI

21.   Chang P, Mei H, Zhao Y, et al. Nature-inspired 3D spiral grass structured graphene quantum dots/MXene nanohybrids with exceptional photothermal-driven pseudo-capacitance improvement. *Adv Sci* 2022;9:e2204086. DOI PubMed PMC

22.   Zhang Y, Ma C, He W, et al. MXene and MXene-based materials for lithium-sulfur batteries. *Prog Nat Sci Mater* 2021;31:501-13. DOI

23.   Dong Y, Zheng S, Qin J, et al. All-MXene-based integrated electrode constructed by Ti_3C_2 nanoribbon framework host and nanosheet interlayer for high-energy-density Li-S batteries. *ACS Nano* 2018;12:2381-8. DOI

24.   Tang H, Li W, Pan L, et al. A robust, freestanding MXene-sulfur conductive paper for long-lifetime Li-S batteries. *Adv Funct Mater* 2019;29:1901907. DOI

25.   Wu Z, Liu X, Shang T, et al. Reassembly of MXene hydrogels into flexible films towards compact and ultrafast supercapacitors. *Adv Funct Mater* 2021;31:2102874. DOI

26.   Xiao Z, Li Z, Li P, Meng X, Wang R. Ultrafine Ti_3C_2 MXene nanodots-interspersed nanosheet for high-energy-density lithium-sulfur batteries. *ACS Nano* 2019;13:3608-17. DOI

27.   Zhang Y, Mu Z, Yang C, et al. Rational design of MXene/1T-2H MoS_2-C nanohybrids for high-performance lithium-sulfur batteries. *Adv Funct Mater* 2018;28:1707578. DOI

28.   Bao W, Liu L, Wang C, Choi S, Wang D, Wang G. Facile Synthesis of crumpled nitrogen-doped MXene nanosheets as a new sulfur host for lithium-sulfur batteries. *Adv Energy Mater* 2018;8:1702485. DOI

29.   Zhang H, Yang L, Zhang P, et al. MXene-Derived Ti_nO_{2n-1} quantum dots distributed on porous carbon nanosheets for stable and long-life Li-S batteries: enhanced polysulfide mediation via defect engineering. *Adv Mater* 2021;33:e2008447. DOI

30.   Tian S, Huang J, Yang H, et al. Self-supporting multicomponent hierarchical network aerogel as sulfur anchoring-catalytic medium for highly stable lithium-sulfur battery. *Small* 2022;18:e2205163. DOI

31.   Zhang C, Cui L, Abdolhosseinzadeh S, Heier J. Two-dimensional MXenes for lithium-sulfur batteries. *InfoMat* 2020;2:613-38. DOI

32.   Zou J, Wu J, Wang Y, et al. Additive-mediated intercalation and surface modification of MXenes. *Chem Soc Rev* 2022;51:2972-90. DOI PubMed

33.   Bae J, Qian Y, Li Y, Zhou X, Goodenough JB, Yu G. Polar polymer-solvent interaction derived favorable interphase for stable lithium metal batteries. *Energy Environ Sci* 2019;12:3319-27. DOI

34.   Fan M, Cui J, Wu J, Vajtai R, Sun D, Ajayan PM. Improving the catalytic activity of carbon-supported single atom catalysts by polynary metal or heteroatom doping. *Small* 2020;16:e1906782. DOI

35.   Liu S, Li J, Yan X, et al. Superhierarchical cobalt-embedded nitrogen-doped porous carbon nanosheets as two-in-one hosts for high-performance lithium-sulfur batteries. *Adv Mater* 2018;30:e1706895. DOI

36.   Naguib M, Kurtoglu M, Presser V, et al. Two-dimensional nanocrystals produced by exfoliation of Ti_3AlC_2. *Adv Mater* 2011;23:4248-53. DOI

37.   Guo Q, Zhang X, Zhao F, et al. Protein-inspired self-healable Ti_3C_2 MXenes/rubber-based supramolecular elastomer for intelligent sensing. *ACS Nano* 2020;14:2788-97. DOI

38.   Peng M, Wang L, Li L, et al. Manipulating the interlayer spacing of 3D MXenes with improved stability and zinc-ion storage capability. *Adv Funct Mater* 2022;32:2109524. DOI

39.   Tan Y, Xu C, Chen G, et al. Synthesis of ultrathin nitrogen-doped graphitic carbon nanocages as advanced electrode materials for supercapacitor. *ACS Appl Mater Interfaces* 2013;5:2241-8. DOI

40.   Chen Y, Li Z, Zhu Y, et al. Atomic Fe dispersed on N-doped carbon hollow nanospheres for high-efficiency electrocatalytic oxygen reduction. *Adv Mater* 2019;31:e1806312. DOI

41.   Bai Y, Liu C, Chen T, et al. MXene-copper/cobalt hybrids via lewis acidic molten salts etching for high performance symmetric supercapacitors. *Angew Chem Int Ed* 2021;60:25318-22. DOI